PAPER

Boosting multi-enzyme cascade activity for glucose biosynthesis by kinetics-oriented grouped immobilization

Ruobing Xin,[a] Yuyao Wang,[c] Qiang Chen, [ID] *[b] Jiangang Yang, [ID] *[c] Yujun Wang [ID] *[a] and Guangsheng Luo [ID] [a]

The biosynthesis of glucose (C6 compound) from CO_2 (C1 compound) represents a highly promising pathway toward sustainable carbon neutrality, requiring ordered multi-enzyme cascade catalysis. However, conventional co-immobilization of multiple enzymes follows an all-in-one approach that struggles to reconcile enzyme compatibility and efficiency. Based on kinetic decoupling, this study introduces a novel strategy of grouped enzyme immobilization to construct a rational multi-enzyme cascade catalytic system. Five enzymes were divided into two groups—upstream (DHAK, TPI, and FSA) and downstream (PGI and G6PP)—and immobilized on the D301 resin to reduce random substrate diffusion and improve cascade efficiency. Compared to all-in-one co-immobilization, this strategy led to a 6.65-fold improvement in glucose yield (508.5 mg L^{-1}) within 2 h. Molecular dynamics simulations revealed that enzymes with higher surface charge form stronger electrostatic bonds with the resin, whereas larger enzymes exhibit weaker binding and greater desorption tendencies, leading to reduced operational stability upon repeated use. The integration of the immobilized enzymes into a packed-bed microreactor enabled stable production of glucose for 12 h of continuous-flow, achieving a space–time yield of 105.9 mg $h^{-1} L^{-1}$. These findings highlight the potential of grouped immobilization on inexpensive carriers for scalable and continuous sugar biomanufacturing.

Green foundation

1. We propose a kinetics-oriented enzyme-grouped immobilization strategy that enhances activity, stability, and reusability in multi-enzyme cascades, offering a scalable, modular platform for green continuous-flow biomanufacturing.

2. The strategy improved glucose yield by 6.65-fold compared to conventional co-immobilization and enabled stable continuous glucose production (105.9 mg $h^{-1} L^{-1}$ for 12 h) using inexpensive, recyclable D301 resin under mild aqueous conditions (pH 7.5, 30 °C).

3. Future improvements include optimizing resin surface chemistry to enhance enzyme binding and reusability, applying grouped immobilization to other biosynthetic pathways, and integrating CO_2-derived feedstocks for fully carbon-neutral carbohydrate synthesis.

Introduction

The upcycling of carbon dioxide (CO_2) into fuels and fine chemicals offers a viable solution to mitigate the climate crisis and alleviate global resource scarcity.[1,2] However, only one-carbon (C1) compounds are currently produced with high efficiency. Given that carbohydrates are crucial for energy storage, human health and nutrition, as well as industrial biomanufacturing,[3,4] the biocatalytic conversion of CO_2-fixed C1 compounds into sugars has attracted growing attention.[5–7] In particular, since the first reported *de novo* synthesis of starch from CO_2 in 2021,[8] artificial carbohydrate synthesis methods, including electro-enzyme and photo-enzyme cascade catalysis, have garnered significant attention.[9–11] The sustainable artificial fixation and conversion of CO_2 into carbohydrates, such as glucose, are considered a pivotal strategy for mitigating climate change and addressing resource depletion.[12] This approach offers new prospects for achieving carbon neutrality[8] and enabling *in situ* energy supply for deep-space exploration.[13–15]

However, the complex stereochemistry and dense functionalization of carbohydrates pose significant challenges

*[a]The State Key Lab of Chemical Engineering, Department of Chemical Engineering, Tsinghua University, Beijing 100084, China.
E-mail: wangyujun@mail.tsinghua.edu.cn*
[b]College of Chemistry and Chemical Engineering, Southwest University, Chongqing 400715, China. E-mail: qiangchen@swu.edu.cn
[c]Tianjin Institute of Industrial Biotechnology, Chinese Academy of Sciences, Tianjin 300308, China
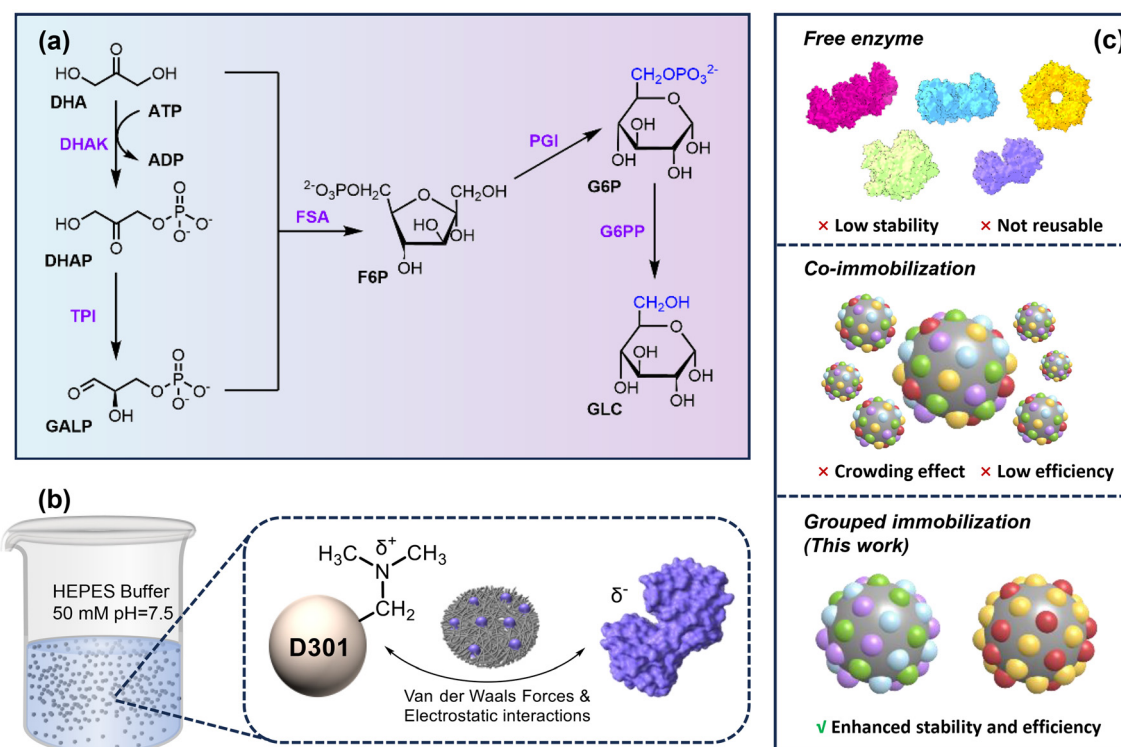
for synthesizing specific monosaccharides *via* conventional chemical methods. In contrast, multi-enzyme cascades offer a promising alternative for highly selective and efficient bottom-up carbohydrate synthesis.[16,17] *In vitro* enzyme cascades exhibit exceptional flexibility, circumventing limitations associated with cell viability, metabolic complexity, and transmembrane transport.[18] Furthermore, by integrating enzymes from diverse sources to construct artificial reaction pathways, these cascades overcome the constraints of natural metabolism, significantly reducing the number of reaction steps while providing key advantages such as high enantio- and stereoselectivity, elevated yields, and reduced downstream processing costs.[19–22]

Nonetheless, the implementation of multi-enzyme cascade systems remains challenging. Free enzymes are intrinsically unstable, sensitive to environmental conditions, and difficult to recycle, leading to high costs and limited operational feasibility.[23,24] Enzyme immobilization transforms enzymes into heterogeneous catalysts by employing carriers or cross-linking agents, thereby significantly enhancing their stability and reusability.[23,25] Common immobilization techniques include physical adsorption, covalent bonding, cross-linking, and encapsulation.[22,26–30] However, immobilized multi-enzyme cascade systems for glucose synthesis face further challenges: (1) the overall reaction rate is highly sensitive to the activity losses of individual enzymes. This sensitivity is exacerbated by the differing compatibilities of enzymes with immobilization methods;[31–33] (2) the high costs of isolating and purifying multi-enzyme systems further limit the practical use of immobilized carrier materials; (3) as cascade complexity increases, mass transfer limitations and random diffusion may offset the benefits of substrate channeling typically conferred by enzyme co-localization.[34]

Physical adsorption based on resin carriers may serve as a feasible solution to these problems, as it relies on non-specific interactions for enzyme binding. Industrial examples such as Novozym 435 demonstrate that polymeric resins can effectively balance catalytic performance and cost-efficiency.[35] The D301 resin is a weakly basic macroporous resin composed of a polystyrene–divinylbenzene matrix functionalized with tertiary amine groups, offering a hydrophobic backbone and a protonatable surface.[36,37] Given the relatively low commercial price of glucose (3–5 USD per kg), the D301 resin (~2.2 USD per kg) offers a clear cost advantage over mesoporous silica (8–20 USD per kg) and biocompatible materials such as ZIF-8 (~130 USD per kg),[38] making it more suitable for enzyme immobilization in glucose-producing multi-enzyme cascade systems.

Herein, we proposed a grouped immobilization strategy for the five-step enzymatic cascade established in our previous study[16] (Scheme 1a). This bottom-up C3-to-C6 biosynthetic route enables glucose production from dihydroxyacetone

Scheme 1 (a) The multi-enzyme cascade system used in this study.[16] The names of reactants or intermediates are written in black, and the names of enzymes are written in purple. DHA: dihydroxyacetone; DHAP: dihydroxyacetone phosphate; GALP: glyceraldehyde 3-phosphate; F6P: fructose-6-phosphate; GLC: glucose; DHAK: dihydroxyacetone kinase; TPI: triosephosphate isomerase; FSA: fructose 6-phosphate aldolase; PGI: glucose-6-phosphate isomerase; G6PP: glucose-6-phosphate phosphatases; (b) schematic of enzyme immobilization on the D301 resin; (c) comparison of free enzymes, co-immobilization, and grouped immobilization strategies.

(DHA), which originates from formaldehyde condensation following CO_2 reduction. In this approach, enzymes were physically adsorbed onto the commercially available weakly basic macroporous resin D301,[36,37] forming enzyme–resin complexes (E@D301). Compared to conventional all-in-one co-immobilization, the grouped strategy enabled the rational spatial distribution of enzymes, enhancing specific activity by optimizing the balance between substrate channeling and molecular diffusion. Enhanced electrostatic interactions between the enzymes and protonated tertiary amines on the resin surface (Scheme 1b) contributed to higher adsorption capacity and stronger binding affinity. Molecular dynamics simulations further revealed that highly charged enzymes favor adsorption *via* coulombic interactions, while bulkier enzymes are more susceptible to desorption due to steric hindrance. Finally, the grouped immobilized enzymes were integrated into a packed-bed microreactor, enabling stable continuous-flow glucose production with improved space–time yield over batch operation.

Results and discussion

Enzyme adsorption on the D301 macroporous resin

The D301 resin is a macroporous anion exchange resin composed of a styrene–divinylbenzene copolymer matrix, functionalized predominantly with tertiary amine groups ($–N(CH_3)_2$). Owing to its positively charged surface potential and aromatic-rich framework, the D301 resin enables enzyme adsorption *via* van der Waals forces, hydrogen bonding, and π–π interactions.

To confirm the successful immobilization of enzymes on the D301 resin, Fourier transform infrared (FT-IR) spectroscopy was conducted (Fig. 1a). A distinct absorption band emerged in the amide I region (1600–1700 cm^{-1}) following enzyme loading, indicating the presence of protein on the resin.[39] Additionally, a pair of sharp peaks appeared in the 2750–2850 cm^{-1} range, which may be attributed to the formation of protonated ammonium species. This suggests electrostatic interactions between the tertiary amine groups on the resin and the carboxyl groups of the enzyme. Furthermore, thermogravimetric analysis (TGA) of the resin before and after immobilization showed distinct differences in mass loss profiles (Fig. 1b). The immobilized samples showed an earlier onset of thermal degradation than that in the bare D301 resin, reflecting the presence of thermally labile protein components. This shift is consistent with the typical decomposition range of proteins (200–300 °C), which is lower than that of the styrene–divinylbenzene polymer backbone. Moreover, the immobilized resin exhibited a higher residual mass at the end of heating, likely due to the carbonization of protein-derived residues forming stable nitrogen-containing structures under inert conditions.[29]

To investigate the structural changes in the D301 resin upon enzyme immobilization, Brunauer–Emmett–Teller (BET) nitrogen adsorption analysis and scanning electron microscopy (SEM) were conducted. The pore size distribution curve (Fig. 1c) indicated a broad range of pore diameters, and SEM images (Fig. 1d) revealed large aggregated pores and mesoporous channels formed by resin fibers. After enzyme adsorption, the average pore diameter increased from 40.02 nm to 45.63 nm (Table S1), which suggests preferential localization of the enzymes within the mesoporous channels.

Accurate knowledge of the size and charge properties of an enzyme is essential for designing effective physical adsorption-based immobilization strategies. These properties depend not only on the primary sequence but also on the oligomeric state of the enzyme under relevant reaction conditions. Size-exclusion chromatography (SEC) was employed to evaluate the apparent molecular size of each enzyme, where the retention time is inversely related to the hydrodynamic volume.[41] Notably, FSA exhibited the shortest retention time among the five enzymes (Fig. 2a), despite having the lowest theoretical molecular weight (23.42 kDa, Table S2). Meanwhile, PGI exhibited a complex peak shape. These results indicate that the enzymes may exist in a multimeric form in solution.

To accurately assess the oligomeric states of the enzymes, homologous protein structures were first identified from the Protein Data Bank (PDB) based on the origin and sequence each enzyme. Structural models were then predicted using AlphaFold3,[42] with most regions exhibiting pLDDT scores above 90, indicating a high level of confidence in the predictions (Fig. S1). Structural alignment with experimentally determined homologs (Fig. S2) showed strong agreement, as reflected by low root mean square deviation (RMSD) values, particularly for TPI, PGI, and G6PP. To validate these predictions and gain further insight into the quaternary structure, single-particle cryo-transmission electron microscopy (cryo-TEM) was performed for DHAK and FSA (Fig. 2b and c).[23] For DHAK, 2D class averages (Fig. S3) revealed a dimeric organization that closely resembled its homologous structure (PDB ID: 1UN8). In the case of FSA, a ring-like architecture was observed, consistent with the tetrameric arrangement found in its homologous crystal structure (PDB ID: 1L6W).

To evaluate enzyme loading and determine the optimal adsorption duration, adsorption kinetic curves for five individual enzymes (Fig. 2d) were obtained by tracking enzyme concentrations over time in HEPES buffer (pH 7.5, 30 °C). The adsorption amount at each time point was quantified using SEC based on peak area ratios (Fig. S4). Adsorption kinetics showed that TPI exhibited the highest adsorption rate and capacity, and FSA displayed the slowest. Interestingly, all enzymes except TPI displayed a linear adsorption phase during the initial 0–10 h, indicative of positive cooperative adsorption[43,44] rather than classical Langmuir-type kinetics. This behavior suggests that pre-adsorbed proteins enhance subsequent adsorption by modifying the local electrostatic environment, consistent with an electrostatic self-assembly mechanism.[45,46] After 12 h, the adsorption curves gradually plateaued, likely owing to multilayer accumulation and steric repulsion, which may impair enzymatic activity and promote desorption.[44] Therefore, an adsorption time of 12 h was selected for all subsequent experiments.
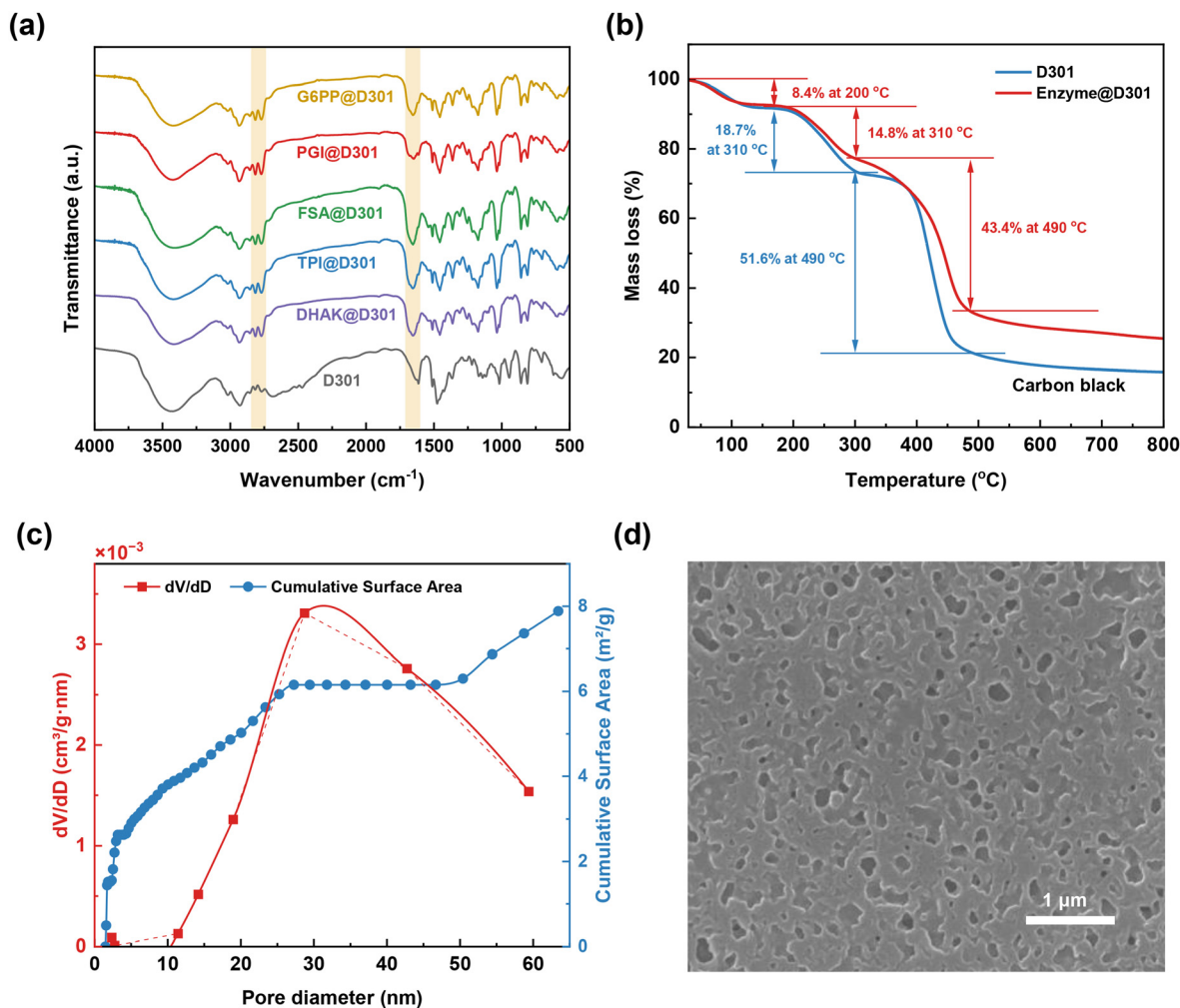
Fig. 1 Characterization of enzyme adsorption on the D301 resin. (a) FT-IR spectrum of D301 before and after enzyme adsorption; (b) TGA curves of the D301 resin before and after enzyme adsorption; (c) BET pore structure analysis of the D301 resin. The average pore diameter increased from 40.02 nm to 45.63 nm; (d) SEM image showing the macroporous structure of the D301 resin.

Enzymes often exhibit highly irregular surface geometries, complicating size estimation. Directly calculating the size from atomic coordinates in protein structure files can significantly overestimate the actual volume, as these coordinates may include substantial void space. To improve the accuracy, we applied principal component analysis (PCA) to determine the principal axes of each enzyme and then reoriented the structure accordingly to calculate the minimum bounding box enclosing the rotated protein (Fig. S5). Based on the amino acid sequences, the surface charge was calculated using the PropKa[40] tool. The analysis revealed that the isoelectric points of the enzymes were predominantly between 4 and 6. At the optimal pH of 7.5, all enzymes exhibited a net negative charge (Fig. 2e). This suggests that the stability of immobilized enzymes can be enhanced by adjusting the solution pH to a mildly alkaline environment, thereby strengthening the electrostatic interactions between enzyme and carrier. The corresponding 3-dimensional enzyme sizes and protein charges are presented in Table 1.

To evaluate the influence of enzyme size and charge on adsorption, we made the following assumptions: (1) enzyme structural integrity remains unchanged during adsorption, implying that no significant unfolding or deformation occurs upon interaction with the resin. (2) Stable adsorption predominantly occurs within mesopores whose dimensions are comparable to those of the enzyme. Therefore, steric accessibility is primarily determined by the maximum cross-sectional area of the enzyme. Under these assumptions, the maximum cross-sectional area (A_{max}) of the enzyme was estimated as the product of the two longest edges of its PCA-derived minimum bounding box. To quantify steric accessibility, we defined a pore accessibility index ($P_{acc} = 1/A_{max}$). A smaller P_{acc} value corresponds to a larger enzyme size, indicating greater steric hindrance in narrow pores. As shown in Fig. 2f, the adsorption capacity decreases with increasing enzyme size, indicating that steric hindrance is a dominant limiting factor. Additionally, surface charge influences adsorption: enzymes with stronger negative surface potential, such as DHAK, experience
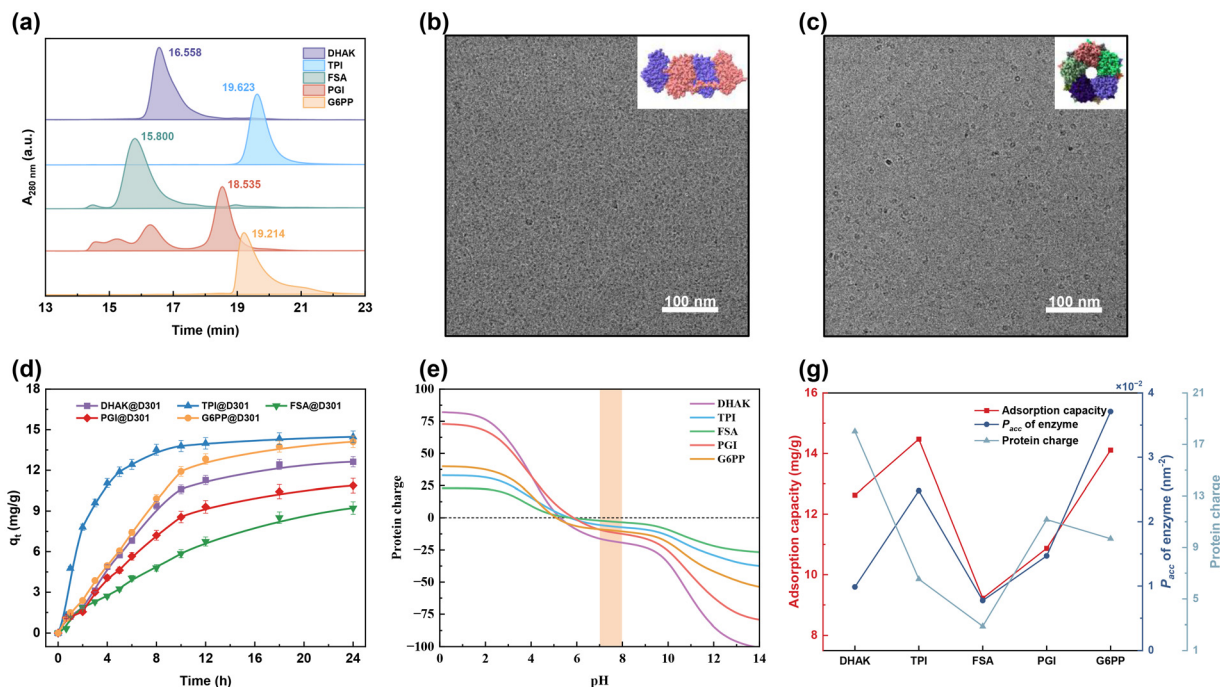
Fig. 2 Effects of enzyme size and charge on adsorption capacity. (a) SEC profiles of the five enzymes used in the reaction system; (b) cryo-TEM image of DHAK; (c) cryo-TEM image of FSA; (d) adsorption kinetics curves of enzymes on the D301 resin; (e) net charge–pH profiles of enzyme subunits calculated using PropKa3;[40] (f) enzyme adsorption capacity, P_{acc} and protein charge.

Table 1 Estimated protein size and net charge at pH = 7.5

Enzymes	Length (Å)	Width (Å)	Height (Å)	Charge
DHAK	144.31	65.81	70.32	−18.01
TPI	80.33	50.17	42.91	−6.54
FSA	111.11	116.35	71.86	−2.87
PGI	85.87	74.89	79.30	−11.17
G6PP	63.32	42.57	39.40	−9.68

enhanced electrostatic interactions with the positively charged D301 resin, resulting in greater adsorption and lower desorption.

Grouped immobilization strategy for a multi-enzyme cascade system

In multi-enzyme cascades, reversible reactions can lead to the accumulation or back-conversion of unstable intermediates.[47] To investigate the influence of intermediate accumulation on reaction efficiency, we grouped the first three enzymes—DHAK, TPI, and FSA—and monitored DHA consumption over time. As shown in Fig. S6, when only DHAK and TPI were present, DHA consumption slowed significantly after 30 min, suggesting that the reaction had reached a dynamic equilibrium owing to the accumulation of the intermediate DHAP and its reversible conversion to GALP. In contrast, inclusion of FSA resulted in a considerable increase in DHA consumption, indicating continuous downstream conversion of GALP and effective relief of product inhibition. These findings demonstrate that co-immobilization of TPI and FSA is crucial for

pulling the equilibrium forward and maintaining a high overall reaction rate (Scheme 2).

The co-immobilization of multiple enzymes presents a fundamental challenge: facilitating efficient substrate channeling while minimizing random diffusion losses. Simply adsorbing all five enzymes onto the D301 resin may not offer optimal performance owing to limitations in both spatial organization and adsorption capacity. Moreover, the limited surface area of D301 restricts total enzyme loading, and increasing the number of enzyme types per carrier reduces the amount of each individual enzyme immobilized, thereby compromising catalytic efficiency. To systematically evaluate the impact of different spatial configurations on overall cascade performance, four enzyme immobilization strategies were designed:
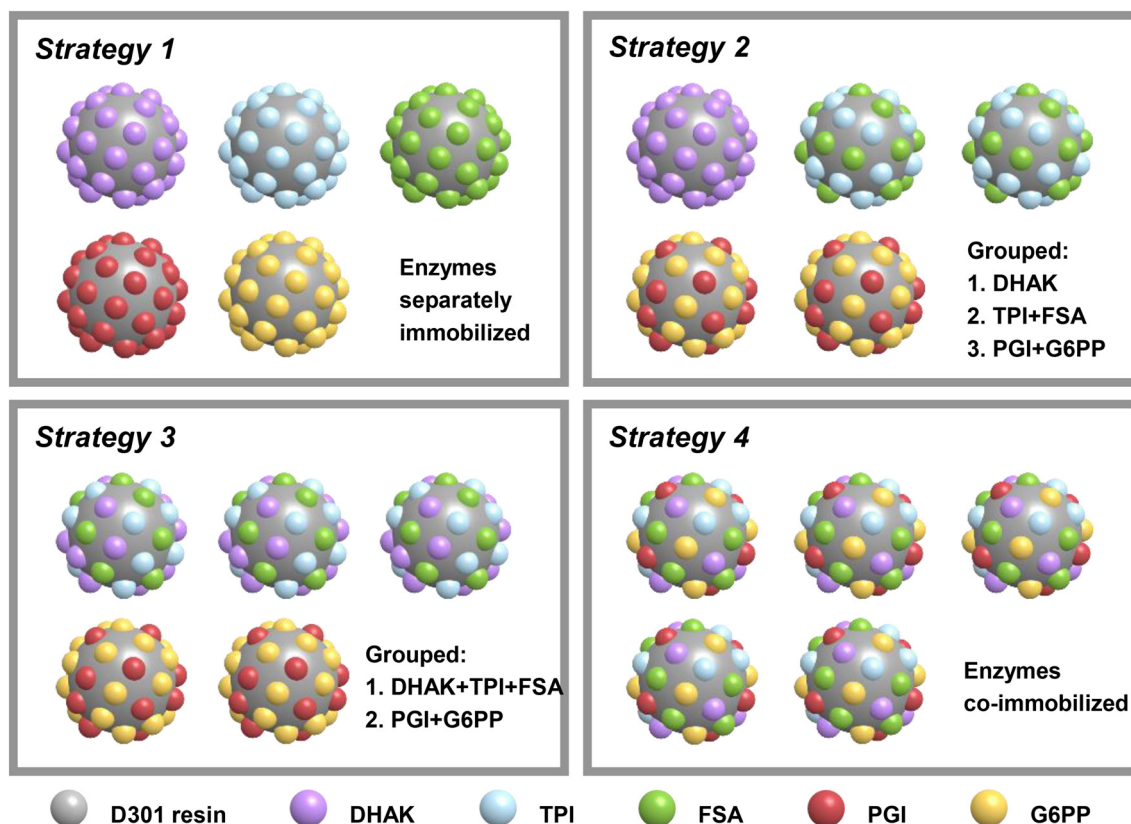
Strategy 1: enzymes were immobilized individually on separate carriers.

Strategy 2: DHAK was immobilized separately; TPI and FSA were co-immobilized; PGI and G6PP were co-immobilized.

Strategy 3: DHAK, TPI, and FSA were co-immobilized; PGI and G6PP were co-immobilized.

Strategy 4: all five enzymes were co-immobilized on a single support.

To assess the activity loss resulting from immobilization, each of the five enzymes was immobilized individually and then combined with the remaining enzymes in the free form for catalytic reaction. As shown in Fig. 3b, DHA conversion remained comparable to that of the fully free-enzyme system, indicating that the initial enzymatic step was largely unaffected. However, the overall yield of GLC decreased signifi-

Scheme 2 Enzyme immobilization strategies used in this study.

cantly, particularly when DHAK or FSA was immobilized. This reduction is likely attributed to increased mass transfer resistance associated with their respective bimolecular reactions, which are more sensitive to diffusional limitations.

Reactions with different immobilization schemes were tested under identical conditions to assess GLC conversion rates (Fig. 3c). As the number of co-immobilized enzymes increased, a noticeable decrease in catalytic efficiency was observed. Notably, when DHAK, TPI, and FSA were immobilized together, the catalytic efficiency decreased by only 9.3% compared to that of when DHAK immobilized separately. By grouping these enzymes, we could evaluate the variation in loading rates. Fig. 3d illustrates that increasing the number of co-immobilized enzymes resulted in a substantial drop in the loading rate of each enzyme. This decline occurred in an approximately proportional manner, indicating that the immobilization process was not significantly influenced by competitive adsorption among the enzymes.

Three-channel laser confocal microscopy was employed to characterize the catalyst prepared using the most effective enzyme co-immobilization strategy (Strategy 3) (Fig. 3e and f).[48] Grinding the D301 resin increased its specific surface area, thereby enhancing its enzyme adsorption capacity and enabling a generally uniform enzyme distribution throughout the material. In the DHAK/TPI/FSA group (Fig. 3e), DHAK and FSA were predominantly localized in the interior of the resin,

whereas TPI was primarily distributed near the surface. Adsorption kinetics analysis (Fig. 2d) suggests that this spatial distribution arises from the relatively small molecular size of TPI, which enables it to access and bind preferentially within mesopores near the resin surface. Consequently, the larger DHAK and FSA molecules are excluded from these surface regions and instead diffuse deeper into the material. In comparison, the PGI/G6PP group (Fig. 3f) exhibited a more homogeneous distribution, consistent with the relatively minor difference in their adsorption rates.

We further evaluated the catalytic performance of fully immobilized enzyme systems. Instead of using combinations of partially immobilized and free enzymes, we prepared D301-based immobilized resins for each enzyme group and conducted the reactions using mixtures of these immobilized resins. As shown in Fig. 3g, the GLC yield from the all-in-one immobilization strategy (Strategy 4) was only 76.5 mg L^{-1}, and the DHA was not fully consumed, suggesting significant limitations owing to reduced enzyme loading and diffusion constraints. Strategy 3 yielded the highest GLC output, demonstrating that this configuration effectively mitigated mass transfer resistance and resulted in a 6.65-fold increase in the GLC yield compared to the five-enzyme co-immobilization strategy.

Reusability tests for enzymes immobilized with different strategies were performed (Fig. 3h and i). The DHA conversion
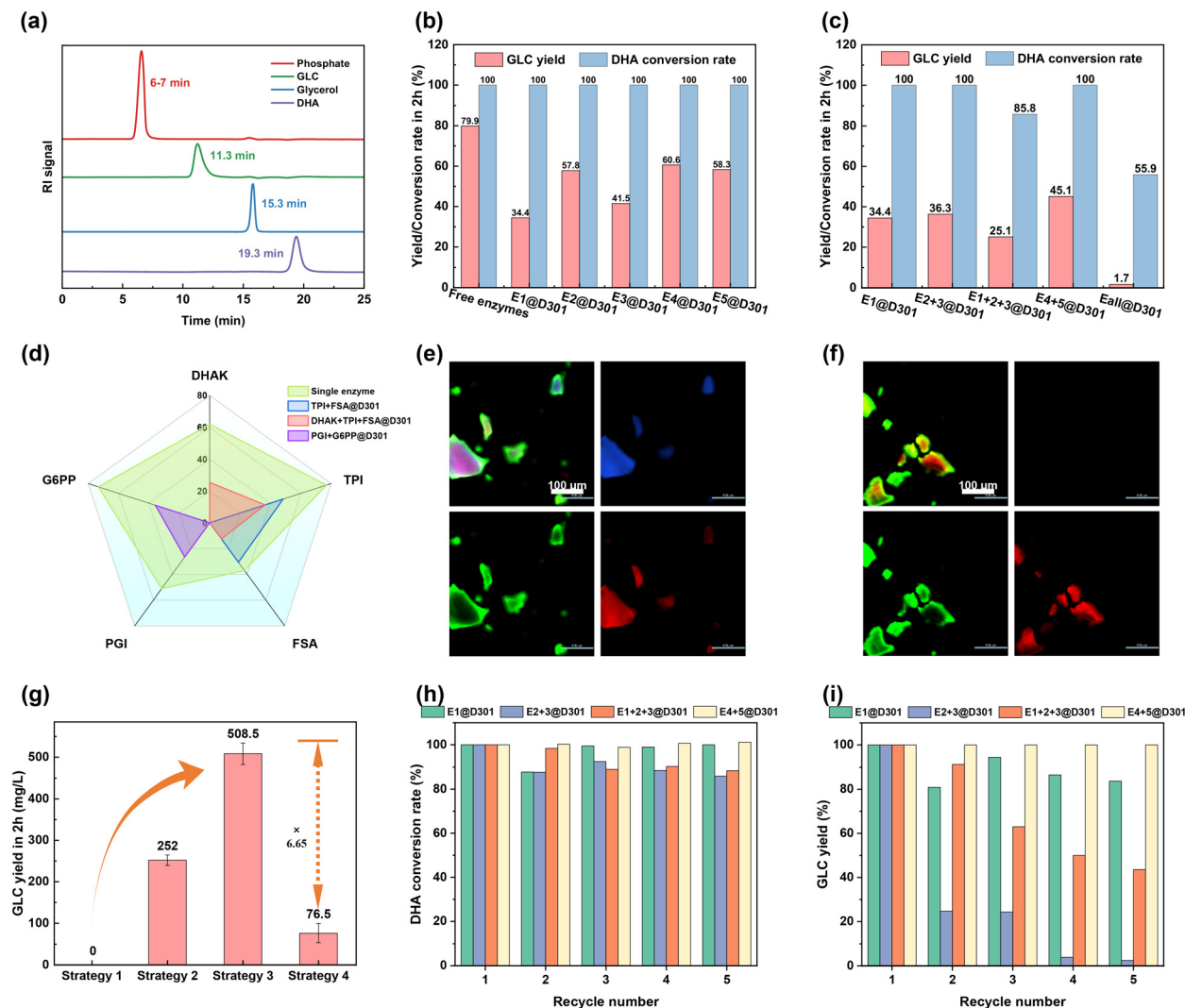
Fig. 3 Reaction results of the multi-enzyme system with grouped immobilization. E1: DHAK, E2: TPI, E3: FSA, E4: PGI, and E5: G6PP; (a) high performance liquid chromatography (HPLC) chromatogram of the reference standards in the reaction system; (b) reaction results of free enzymes and single-enzyme immobilization; (c) reaction results of different grouped immobilization strategies; (d) enzyme immobilization efficiency under different grouped adsorption strategies at an initial enzyme concentration of 2 mg mL^{-1}; (e) confocal microscopy images of E1 + 2 + 3@D301 with AMCA-X SE-labelled DHAK (blue), FITC-labelled TPI (green) and RhB-labelled FSA (red); (f) confocal microscopy images of E4 + 5@D301 with FITC-labelled PGI (green) and RhB-labelled G6PP (red); (g) comparison of GLC yield across different strategies; (h and i) reusability of grouped immobilization schemes, normalized to the activity of the first cycle.

rate remained relatively stable across all groups, indicating good stability and activity of DHAK. Notably, the PGI + G6PP@D301 group maintained nearly the same catalytic performance after five cycles as in the initial run. This excellent stability may be attributed to two factors: first, both enzymes are derived from thermophilic organisms and possess inherent structural stability; second, their moderate molecular size and surface charge likely promote more stable interactions with the D301 resin. In contrast, the groups containing DHAK, TPI, and FSA exhibited a rapid decline in the GLC yield over repeated cycles. DHAK@D301 retained approximately 80% of its activity after five cycles, owing to its relatively stronger interaction with the carrier. In contrast, the TPI + FSA@D301 group

lost nearly its catalytic activity after five cycles, suggesting significantly weaker binding and potential structural instability under repeated use. The DHAK + TPI + FSA@D301 group showed a slower decline in activity, indicating that the grouping strategy partially mitigated enzyme deactivation. Nevertheless, its activity after five cycles was only around 40% of that observed in the first cycle.

Molecular dynamics simulations of DHAK and FSA adsorption on the D301 resin

To investigate the contribution of electrostatic interactions to protein adsorption and to gain mechanistic insight into the observed decline in enzyme reusability upon immobilization, a

molecular model of the D301 resin was constructed by cross-linking styrene and divinylbenzene. Molecular dynamics (MD) simulations of 100 ns were then conducted to explore the adsorption behaviors of DHAK and FSA on the resin surface.[49,50] These two enzymes were selected as representative cases: DHAK exhibits the highest surface charge among the five enzymes, and FSA is the largest in molecular size; both catalyze the key steps in the cascade reaction and are thus critical to the overall system performance.

Snapshot images of the adsorption trajectories are shown in Fig. 4a and b. DHAK retained a relatively stable conformation during adsorption, whereas FSA underwent a significant reorientation from a "lying-down" to a "side-standing" configuration. Electrostatic potential maps calculated using Adaptive Poisson–Boltzmann Solver (APBS, Fig. S7) revealed a broad distribution of negatively charged regions across the DHAK surface, favoring extended planar interactions with the positively charged resin. In contrast, the negative charge on

FSA was predominantly localized to its periphery, leading to a preferential side-on binding mode.

RMSD and root-mean-square fluctuation (RMSF) analyses (Fig. 4c) demonstrated that both DHAK and FSA maintained structural integrity throughout the 100 ns adsorption simulations.[49] No significant conformational rearrangements were observed, indicating that the immobilization process did not disrupt their overall structural frameworks. This finding was corroborated by secondary structure analysis using the DSSP algorithm (Fig. S8), which revealed minimal alterations in the secondary structure elements of the enzyme. Notably, regions with elevated RMSF values corresponded primarily to flexible, unstructured coil regions.

To gain deeper insights into the nature of enzyme–resin interactions, van der Waals and electrostatic forces were quantitatively evaluated. As shown in Fig. 4e, both Lennard-Jones (L-J) and coulombic potential energies decreased progressively over time, reflecting the increasing strength of interactions as
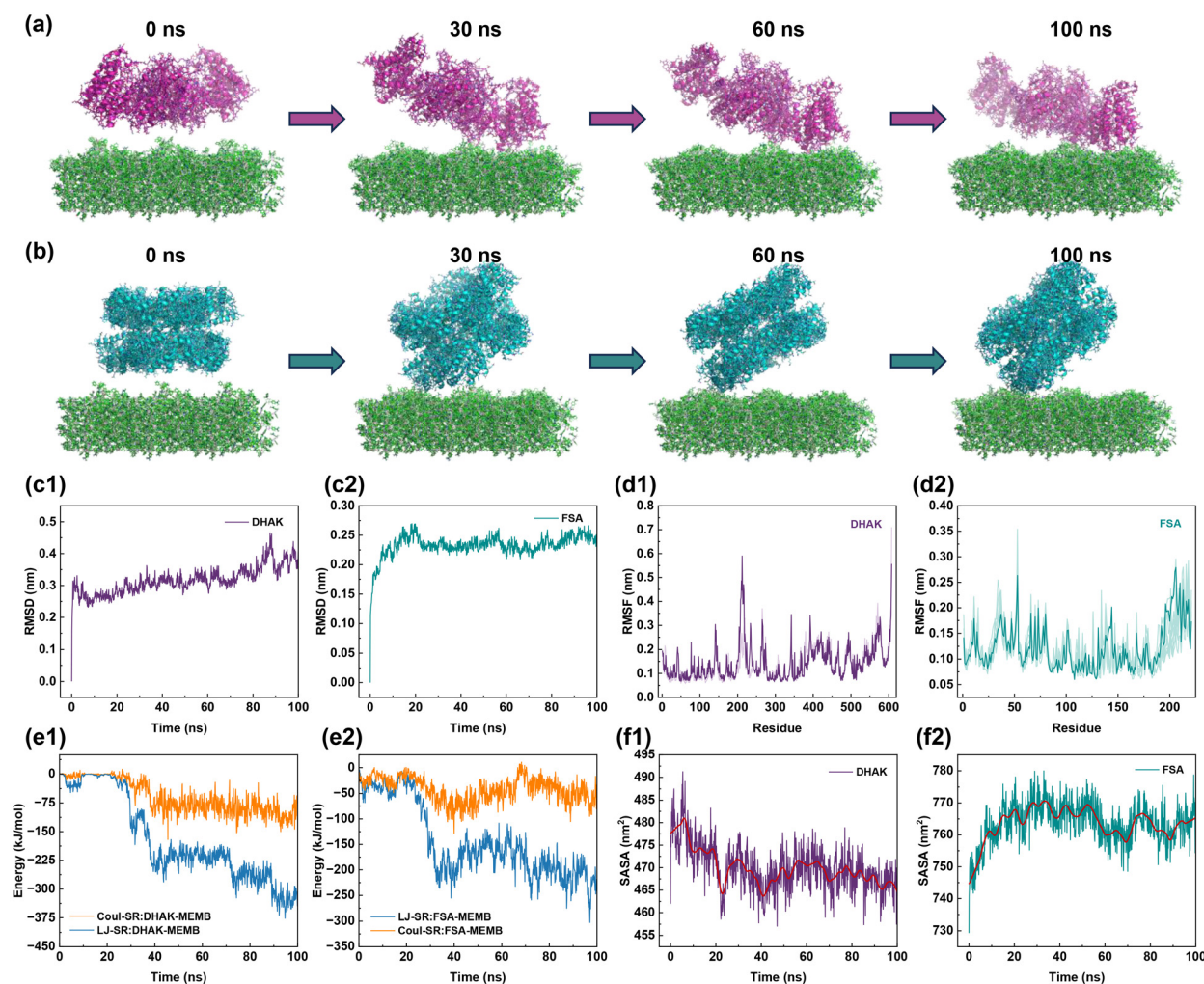

Fig. 4 MD simulations of DHAK and FSA adsorption on the D301 resin. (a) Snapshot images of DHAK at different time points during the simulation on the D301 surface; (b) snapshot images of FSA at different time points during the simulation on the D301 surface; (c) RMSD curves of DHAK and FSA; (d) RMSF curves of DHAK and FSA; (e) Lennard-Jones and coulombic interaction energies between DHAK/FSA and the D301 surface during the simulation; (f) SASA of DHAK and FSA during the simulation.

the enzymes approached and adsorbed onto the D301 polymer surface. During the stable adsorption phase (40–100 ns), DHAK displayed significantly stronger interactions, with average L-J and coulombic potentials of -250.28 kJ mol^{-1} and -87.98 kJ mol^{-1}, respectively. In comparison, FSA exhibited weaker interactions, with corresponding values of -186.48 kJ mol^{-1} and -47.92 kJ mol^{-1}. These differences highlight the stronger binding affinity of DHAK, which can be attributed to its smaller molecular size and more extensively distributed negative surface charge. Together, these characteristics promote more stable and extensive contact with the D301 surface, thereby enhancing adsorption capacity.

Further evidence was obtained from solvent-accessible surface area (SASA) analysis, which characterizes the extent of molecular surface exposure to the solvent (Fig. 4f). For DHAK, the SASA decreased from 477.67 nm^2 at the start of the simulation to 464.53 nm^2 by the end, suggesting that surface atoms at the enzyme–resin interface became progressively buried upon adsorption. In contrast, FSA exhibited an increase in SASA from 744.54 nm^2 to 765.35 nm^2 over the same period, indicating enhanced surface exposure. This elevated exposure may reflect weaker anchoring to the resin and increased interaction with the aqueous environment, which could facilitate desorption. These observations provide a plausible explanation for the lower reusability of FSA in immobilized systems and reinforce the conclusion that both molecular size and surface charge distribution are critical determinants of adsorption strength and stability.
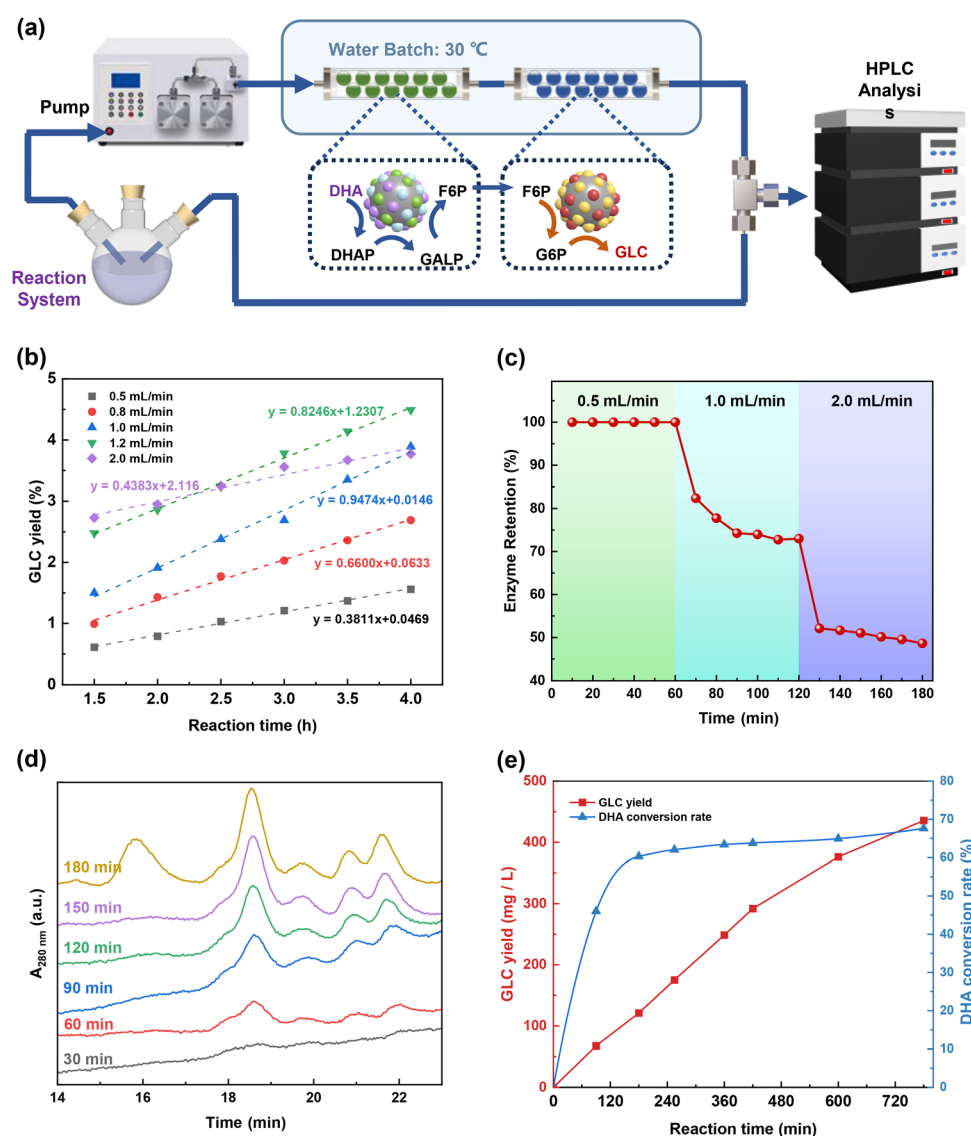

Fig. 5 Continuous-flow process and reaction results. (a) Scheme of the continuous-flow micro-packed bed reactor equipped with immobilized enzymes for glucose synthesis and real-time HPLC analysis; (b) GLC yield *vs.* time at different flow rates; (c) time-dependent enzyme retention determined by the Bradford assay under varying flow conditions; (d) SEC analysis of samples collected at different flow durations; (e) long-term reaction results at a flow rate of 1.0 mL min^{-1}.

Flow synthesis of glucose in a packed-bed microreactor

A continuous-flow system was constructed based on the developed enzyme immobilization strategy (Fig. 5a). The reaction was carried out in a micro-scale packed-bed reactor maintained at 30 °C in a water bath. The effect of flow rate on the reactor performance was investigated, as shown in Fig. 5b. At all tested flow rates, the GLC yield increased linearly with time, and the slope of the fitted curve—representing reaction rate—increased with a flow rate up to 1.0 mL min^{-1}. However, at higher flow rates (*e.g.*, 2.0 mL min^{-1}), the slope declined significantly, and the reaction curve deviated from the expected trend.

To investigate the cause of decreased glucose yield under high flow conditions, a continuous-flow experiment was performed using the micro-packed bed, in which the flow rate was incrementally increased every hour. Enzyme concentrations in the downstream effluent were monitored to assess potential enzyme loss. Protein content in the effluent was quantified using the Bradford assay to calculate enzyme retention rates (Fig. 5c and d), while SEC was used to qualitatively identify the enzyme species present. At 0.5 mL min^{-1}, no significant enzyme loss was observed. However, when the flow rate increased to 1.0 mL min^{-1}, the retention rate dropped sharply to 72%, likely due to shear-induced desorption of weakly bound enzymes.[51] SEC analysis revealed a dominant peak at 18.5 min (corresponding to PGI) and new peaks beyond 20 min, which may indicate structural degradation into subunits or fragments. At 2.0 mL min^{-1}, enzyme retention further declined to 50% and continued decreasing gradually. A distinct peak appeared at 15.8 min (corresponding to FSA), along with intensified fragment peaks. These results suggest that reduced glucose yield at high flow rates is primarily caused by enzyme desorption and structural destabilization, particularly affecting enzymes like PGI and FSA with weaker resin interactions (Fig. 2d and f).

Based on these results, 1.0 mL min^{-1} was identified as the optimal flow rate. The long-term operational stability of the packed-bed system was also assessed (Fig. 5e). The reactor maintained consistent catalytic activity for over 720 min, achieving a space–time yield of 105.9 mg h^{-1} L^{-1}, indicating good stability and practical potential for continuous biocatalytic glucose production. Compared to previously reported *de novo* monosaccharide synthesis routes (Table S4), the STY achieved in our packed-bed microreactor is comparable to continuous-flow systems based on tandem CSTRs (105 mg h^{-1} L^{-1} for L-sorbose production from CO$_2$),[11] and shows advantages in operational stability, enzyme reuse, and process intensification.

Conclusions

In this study, we developed a cost-effective and modular grouped immobilization strategy for organizing a five-enzyme cascade on the macroporous D301 resin, enabling efficient conversion of DHA into glucose. By leveraging pH-tuned electrostatic interactions, the approach enhanced enzyme retention and minimized competitive adsorption. Through comparison of different grouping patterns based on kinetic decoupling, a 3 + 2 configuration was identified as the most efficient. These two groups were immobilized separately on the D301 resin, effectively reducing random substrate diffusion and enhancing overall cascade performance. Compared to all-in-one co-immobilization, the grouped strategy significantly improved catalytic efficiency, yielding 508.5 mg L^{-1} glucose within 2 h—6.65 times higher than that of the co-immobilized system.

MD simulations revealed that enzymes with smaller size and higher surface charge exhibit stronger and more stable electrostatic interactions with the resin, while larger enzymes are more prone to desorption, compromising operational stability during reuse. When integrated into a packed-bed microreactor, the space–time yield initially increased with the flow rate, reaching a maximum at 1.0 mL min^{-1}, but declined at higher rates, which was attributed to the desorption and partial structural disruption of weakly bound enzymes. When operated at the optimal flow rate, the immobilized system enabled continuous glucose production for 720 min with a space–time yield of 105.9 mg h^{-1} L^{-1}, demonstrating long-term operational stability.

This work explores the fundamental principles of the DHA-to-glucose multi-enzyme cascade and introduces a straightforward grouped immobilization strategy on the cost-effective D301 carrier. This approach enhances enzyme adsorption efficiency and significantly improves the performance of multi-enzyme cascades under continuous-flow conditions. Future work will focus on tuning the carrier surface chemistry and structure to further enhance the stability of sensitive enzymes. Moreover, this immobilization strategy holds potential for application in other high-value biosynthetic pathways, particularly for the *in vitro* synthesis of sugar alcohols (*e.g.*, inositol, D-mannitol, and erythritol)[52,53] and functional rare sugars (*e.g.*, D-allulose and D-tagatose).[17,54]

Conflicts of interest

There are no conflicts to declare.

Data availability

Data will be made available on request. The data that support the findings of this study are available from the corresponding authors on reasonable request.

Additional data that support the findings of this study, including detailed experimental protocols, supplementary figures and tables, are available in the SI file. See DOI: **https://doi.org/10.1039/d5gc03123k**.

Acknowledgements

References

1 S. Morales-delaRosa, J. M. Campos-Martin and J. L. G. Fierro, *Cellulose*, 2014, **21**, 2397–2407.

2 T. A. Saleh, *RSC Adv.*, 2022, **12**, 23869–23888.

3 P. L. Keeling and A. M. Myers, *Annu. Rev. Food Sci. Technol.*, 2010, **1**, 271–303.

4 A. C. WeymouthWilson, *Nat. Prod. Rep.*, 1997, **14**, 99–110.

5 J. G. Yang, S. S. Sun, Y. Men, Y. Zeng, Y. M. Zhu, Y. X. Sun and Y. H. Ma, *Catal. Sci. Technol.*, 2017, **7**, 3459–3463.

6 Y. Y. Qiao, W. Y. Ma, S. J. Zhang, F. Guo, K. Liu, Y. J. Jiang, Y. X. Wang, F. X. Xin, W. M. Zhang and M. Jiang, *Synth. Syst. Biotechnol.*, 2023, **8**, 578–583.

7 Q. Liu, L. P. Wu, R. Jackstell and M. Beller, *Nat. Commun.*, 2015, **6**, 5933.

8 T. Cai, H. B. Sun, J. Qiao, L. L. Zhu, F. Zhang, J. Zhang, Z. J. Tang, X. L. Wei, J. G. Yang, Q. Q. Yuan, W. Y. Wang, X. Yang, H. Y. Chu, Q. Wang, C. You, H. W. Ma, Y. X. Sun, Y. Li, C. Li, H. F. Jiang, Q. H. Wang and Y. H. Ma, *Science*, 2021, **373**, 1523–1527.

9 T. T. Zheng, M. L. Zhang, L. H. Wu, S. Y. Guo, X. J. Liu, J. K. Zhao, W. Q. Xue, J. W. Li, C. X. Liu, X. Li, Q. Jiang, J. Bao, J. Zeng, T. Yu and C. Xia, *Nat. Catal.*, 2022, **5**, 388–396.

10 S. S. Zhang, J. H. Sun, D. D. Feng, H. L. Sun, J. Y. Cui, X. X. Zeng, Y. N. Wu, G. D. Luan and X. F. Lu, *Nat. Commun.*, 2023, **14**, 3425.

11 G. Y. Liu, Y. Zhong, Z. H. Liu, G. Wang, F. Gao, C. Zhang, Y. J. Wang, H. W. Zhang, J. Ma, Y. G. Hu, A. B. Chen, J. Y. Pan, Y. Z. Min, Z. Y. Tang, C. Gao and Y. J. Xiong, *Nat. Commun.*, 2024, **15**, 2636.

12 S. Cestellos-Blanco, S. Louisia, M. B. Ross, Y. F. Li, N. E. Soland, T. C. Detomasi, J. N. C. Spradlin, D. K. Nomura and P. D. Yang, *Joule*, 2022, **6**, 2304–2323.

13 J. B. G. Martinez, K. A. Alvarado, X. Christodoulou and D. C. Denkenberger, *J. CO2 Util.*, 2021, **53**, 101726.

14 A. J. Berliner, J. M. Hilzinger, A. J. Abel, M. J. McNulty, G. Makrygiorgos, N. J. H. Averesch, S. Sen Gupta, A. Benvenuti, D. F. Caddell, S. Cestellos-Blanco, A. Doloman, S. Friedline, D. A. Ho, W. Y. Gu, A. Hill, P. Kusuma, I. Lipsky, M. Mirkovic, J. L. Meraz, V. Pane, K. B. Sander, F. Z. Shi, J. M. Skerker, A. Styer, K. Valgardson, K. Wetmore, S. G. Woo, Y. A. Xiong, K. Yates, C. Zhang, S. Y. Zhen, B. Bugbee, D. S. Clark, D. Coleman-Derr, A. Mesbah, S. Nandi, R. M. Waymouth, P. D. Yang, C. S. Criddle, K. A. McDonald, L. C. Seefeldt, A. A. Menezes and A. P. Arkin, *Front. Astron. Space*, 2021, **8**, 711550.

15 C. V. Manning, C. P. McKay and K. J. Zahnle, *Icarus*, 2006, **180**, 38–59.

16 J. A. Yang, W. Song, T. Cai, Y. Y. Wang, X. W. Zhang, W. Y. Wang, P. Chen, Y. Zeng, C. Li, Y. X. Sun and Y. H. Ma, *Sci. Bull.*, 2023, **68**, 2370–2381.

17 J. G. Yang, T. Zhang, C. Y. Tian, Y. M. Zhu, Y. Zeng, Y. Men, P. Chen, Y. X. Sun and Y. H. Ma, *Biotechnol. Adv.*, 2019, **37**(7), 107406.

18 E. T. Hwang and S. Lee, *ACS Catal.*, 2019, **9**, 4402–4425.

19 Z. L. Wang, B. S. Sekar and Z. Li, *Bioresour. Technol.*, 2021, **323**, 124551.

20 R. J. Conrado, J. D. Varner and M. P. DeLisa, *Curr. Opin. Biotechnol.*, 2008, **19**, 492–499.

21 S. F. Mayer, W. Kroutil and F. Kurt, *Chem. Soc. Rev.*, 2001, **30**, 332–339.

22 Y. L. Hu, L. M. Dai, D. H. Liu and W. Du, *Green Chem.*, 2018, **20**, 4500–4506.

23 Q. Chen, G. Qu, X. Li, M. J. Feng, F. Yang, Y. J. Li, J. C. Li, F. F. Tong, S. Y. Song, Y. J. Wang, Z. T. Sun and G. S. Luo, *Nat. Commun.*, 2023, **14**, 2117.

24 R. H. Y. Chang, J. Jang and K. C. W. Wu, *Green Chem.*, 2011, **13**, 2844–2850.

25 R. A. Sheldon, A. Basso and D. Brady, *Chem. Soc. Rev.*, 2021, **50**, 5850–5862.

26 J. Y. Zhang, J. F. Lovell, J. F. Shi and Y. M. Zhang, *Bmemat*, 2025, **3**(1), e12080.

27 F. Yang, P. Zhang, J. Qu, Y. Cai, X. Yang, C. M. Li and J. Hu, *Nano Energy*, 2025, **136**, 110682.

28 X. Wu, J. Ge, C. Yang, M. Hou and Z. Liu, *Chem. Commun.*, 2015, **51**, 13408–13411.

29 F. Lyu, Y. Zhang, R. N. Zare, J. Ge and Z. Liu, *Nano Lett.*, 2014, **14**, 5761–5765.

30 P. Luan, Y. Li, C. Huang, L. Dong, T. Ma, J. Liu, J. Gao, Y. Liu and Y. Jiang, *ACS Catal.*, 2022, **12**(13), 7550–7558.

31 S. Y. Chen, W. S. Lo, Y. D. Huang, X. M. Si, F. S. Liao, S. W. Lin, B. P. Williams, T. Q. Sun, H. W. Lin, Y. Y. An, T. Sun, Y. H. Ma, H. C. Yang, L. Y. Chou, F. K. Shieh and C. K. Tsung, *Nano Lett.*, 2020, **20**, 6630–6635.

32 W. B. Liang, H. S. Xu, F. Carraro, N. K. Maddigan, Q. W. Li, S. G. Bell, D. M. Huang, A. Tarzia, M. B. Solomon, H. Amenitsch, L. Vaccari, C. J. Sumby, P. Falcaro and C. J. Doonan, *J. Am. Chem. Soc.*, 2019, **141**, 2348–2355.

33 G. S. Chen, X. X. Kou, S. M. Huang, L. J. Tong, Y. J. Shen, W. S. Zhu, F. Zhu and G. F. Ouyang, *Angew. Chem., Int. Ed.*, 2020, **59**, 2867–2874.

34 M. B. Quin, K. K. Wallin, G. Zhang and C. Schmidt-Dannert, *Org. Biomol. Chem.*, 2017, **15**, 4260–4271.

35 C. Ortiz, M. L. Ferreira, O. Barbosa, J. C. S. dos Santos, R. C. Rodrigues, A. Berenguer-Murcia, L. E. Briand and R. Fernandez-Lafuente, *Catal. Sci. Technol.*, 2019, **9**, 2380–2420.

36 C. H. Li and D. M. Jia, *Chin. J. Chem. Eng.*, 2016, **24**, 1522–1526.

37 F. Q. An, H. F. Li, X. D. Guo, X. Y. Xue, Y. Wang, T. P. Hu and J. F. Gao, *Sep. Sci. Technol.*, 2019, **54**, 2361–2373.

38 A. Deacon, L. Briquet, M. Malankowska, F. Massingberd-Mundy, S. Rudic, T. L. Hyde, H. Cavaye, J. Coronas, S. Poulston and T. Johnson, *Commun. Chem.*, 2022, **5**, 18.

39 Z. X. Guo, W. X. Kong, L. Y. Zhou, Y. He, L. Ma, G. H. Liu, Y. T. Liu and Y. J. Jiang, *ACS Catal.*, 2025, **15**, 3955–3966.

40 M. H. M. Olsson, C. R. Sondergaard, M. Rostkowski and J. H. Jensen, *J. Chem. Theory Comput.*, 2011, **7**, 525–537.

41 D. Gervais, A. Downer, D. King, P. Kanda, N. Foote and S. Smith, *J. Pharm. Biomed. Sci.*, 2017, **139**(30), 215–220.

42 J. Abramson, J. Adler, J. Dunger, R. Evans, T. Green, A. Pritzel, O. Ronneberger, L. Willmore, A. J. Ballard, J. Bambrick, S. W. Bodenstein, D. A. Evans, C. C. Hung, M. O'Neill, D. Reiman, K. Tunyasuvunakool, Z. Wu, A. Zemgulyte, E. Arvaniti, C. Beattie, O. Bertolli, A. Bridgland, A. Cherepanov, M. Congreve, A. I. Cowen-Rivers, A. Cowie, M. Figurnov, F. B. Fuchs, H. Gladman, R. Jain, Y. A. Khan, C. M. R. Low, K. Perlin, A. Potapenko, P. Savy, S. Singh, A. Stecula, A. Thillaisundaram, C. Tong, S. Yakneen, E. D. Zhong, M. Zielinski, A. Zídek, V. Bapst, P. Kohli, M. Jaderberg, D. Hassabis and J. M. Jumper, *Nature*, 2024, **630**, 493–500.

43 R. C. Chatelier and A. P. Minton, *Biophys. J.*, 1996, **71**, 2367–2374.

44 M. Rabe, D. Verdes and S. Seeger, *Adv. Colloid Interface Sci.*, 2011, **162**, 87–106.

45 V. Ball and J. J. Ramsden, *J. Phys. Chem. B*, 1997, **101**, 5465–5469.

46 E. N. Vasina and P. Déjardin, *Langmuir*, 2004, **20**, 8699–8706.

47 C. T. Walsh and B. S. Moore, *Angew. Chem., Int. Ed.*, 2019, **58**, 6846–6879.

48 W. H. Chen, M. Vázquez-González, A. Zoabi, R. Abu-Reziq and I. Willner, *Nat. Catal.*, 2018, **1**, 689–695.

49 J. Zhou, J. Zheng and S. Y. Jiang, *J. Phys. Chem. B*, 2004, **108**, 17418–17424.

50 X. B. Quan, J. Liu and J. Zhou, *Curr. Opin. Colloid Interface Sci.*, 2019, **41**, 74–85.

51 Q. Chen, G. S. Luo and Y. J. Wang, *Green Chem.*, 2021, **23**, 7074–7083.

52 C. You, T. Shi, Y. J. Li, P. P. Han, X. G. Zhou and Y. H. P. Zhang, *Biotechnol. Bioeng.*, 2017, **114**, 1855–1864.

53 X. L. Wei, Q. Z. Li, C. C. Hu and C. You, *Appl. Microbiol. Biotechnol.*, 2021, **105**, 1913–1924.

54 T. B. Granström, G. Takata, M. Tokuda and K. Izumori, *J. Biosci. Bioeng.*, 2004, **97**, 89–94.